



### **Science Arts & Métiers (SAM)**

is an open access repository that collects the work of Arts et Métiers Institute of Technology researchers and makes it freely available over the web where possible.

This is an author-deposited version published in: <https://sam.ensam.eu>  
Handle ID: <http://hdl.handle.net/10985/12357>

#### **To cite this version :**

Léo MORIN, Jean-Baptiste LEBLOND, Dirk MOHR, Djimedo KONDO - Prediction of shear-dominated ductile fracture in a butterfly specimen using a model of plastic porous solids including void shape effects - European Journal of Mechanics - A/Solids - Vol. 61, p.433-442 - 2017

Any correspondence concerning this service should be sent to the repository

Administrator : [scienceouverte@ensam.eu](mailto:scienceouverte@ensam.eu)



# Prediction of shear-dominated ductile fracture in a butterfly specimen using a model of plastic porous solids including void shape effects

Léo Morin <sup>a, b, \*</sup>, Jean-Baptiste Leblond <sup>a</sup>, Dirk Mohr <sup>c</sup>, Djimédo Kondo <sup>a</sup>

<sup>a</sup> Sorbonne Universités, UPMC Univ Paris 06, CNRS, UMR 7190, Institut Jean Le Rond d'Alembert, F-75005, Paris, France

<sup>b</sup> Laboratoire de Mécanique et d'Acoustique, CNRS, UPR 7051, Aix-Marseille Univ, Centrale Marseille, 4 impasse Nikola Tesla, CS 40006, 13453, Marseille Cedex 13, France

<sup>c</sup> ETH Zurich, Department of Mechanical and Process Engineering, Switzerland

## A B S T R A C T

The aim of this paper is to investigate ductile failure under shear-dominated loadings using a model of plastic porous solids incorporating void shape effects. We use the model proposed by (Madou and Leblond, 2012a,b; Madou et al., 2013; Madou and Leblond, 2013) to study the fracture of butterfly specimens subjected to combined tension and shear. This model is able to reproduce, for various loading conditions, the macroscopic softening behavior and the location of cracks observed in experiments performed by Dunand and Mohr (2011a,b). Void shape effects appear to have a very significant influence on ductile damage at low stress triaxiality.

## Keywords:

Porous ductile materials  
Void shape effects  
Shear loadings  
Numerical simulations  
Experimental results

## 1. Introduction

Ductile fracture is the most common mode of failure of metals and alloys at room and high temperatures. This type of fracture arises from the successive nucleation, growth and coalescence of voids. Although its understanding and modeling have known tremendous progress during the last fifty years (see Benzerga and Leblond (2010) and Pineau et al. (2016) for recent reviews of the topic), many open questions still remain. Among the remaining challenges, the prediction of ductile fracture under conditions of low stress triaxiality (ratio of the mean and von Mises equivalent stresses) has recently been the focus of extensive studies.

From the *experimental* point of view, several recent studies have investigated the initiation of ductile fracture under combined tensile and shear loading (e.g. Mohr and Henn (2007); Barsoum and Faleskog (2007a); Dunand and Mohr (2011a,b); Graham et al. (2012); Haltom et al. (2013); Ghahremaninezhad and Ravi-Chandar (2013); Faleskog and Barsoum (2013); Papisidero et al. (2015)). It is worth noting that all these studies confirm the absence

of significant void growth away from the final fracture surface under conditions of dominant shear. It may thus be speculated that macroscopic softening due to important changes of the shape of the voids is responsible for ductile fracture in shear experiments.

From the *numerical* point of view, important efforts have also been dedicated to the study of ductile fracture in finite element micromechanical simulations of elementary porous cells subjected to shear-dominated loadings (Barsoum and Faleskog, 2007b; Leblond and Mottet, 2008; Tvergaard, 2009; Tvergaard and Nielsen, 2010; Scheyvaerts et al., 2011; Nielsen et al., 2012; Tvergaard, 2012, 2015; Dunand and Mohr, 2014). These studies have shown that under conditions of dominant shear, voids rotate, flatten and close up in a mechanism of “mesoscopic strain localization” between voids,<sup>1</sup> leading to macroscopic softening. When the triaxiality increases, a continuous transition is observed between this mechanism and the necking of the ligaments between neighboring voids leading to standard coalescence, as observed numerically in the work of Koplik and Needleman (1988), followed by many others.

\* Corresponding author. Sorbonne Universités, UPMC Univ Paris 06, CNRS, UMR 7190, Institut Jean Le Rond d'Alembert, F-75005, Paris, France.  
E-mail address: [leo.morin@ens-cachan.fr](mailto:leo.morin@ens-cachan.fr) (L. Morin).

<sup>1</sup> The adjective “mesoscopic” means that localization occurs neither at the microscopic scale nor at the macroscopic scale of the void spacing, but at the intermediate scale of the void diameter.

From the *theoretical* point of view, a lot of progress has been made on the modeling of ductile fracture since the seminal works of [McClintock \(1968\)](#) and [Rice and Tracey \(1969\)](#), who studied the growth of a single cavity in an infinite plastic matrix and evidenced, for the first time, the essential impact of triaxiality upon the void growth rate. Their work laid the foundations of the modeling of void growth, and was followed by the major contribution of [Gurson \(1977\)](#), who combined homogenization and limit-analysis of a spherical finite cell containing a spherical void to derive a complete and consistent model of plastic porous materials. Due to its intrinsic limitation to spherical voids, Gurson's model cannot predict any softening for a zero triaxiality, because the softening arises in this model only from the increase of the porosity which is nil under such conditions. Several classes of remedies have therefore been proposed in order to account for the softening observed under shear-dominated loadings:

- (1) The first class is based on a heuristic modification of the evolution equation of the porosity ([Nahshon and Hutchinson, 2008](#); [Xue, 2008](#)). This equation is modified by including an extra term that does not vanish when the triaxiality is zero; this term thus generates some softening in shear. With this modification, the porosity is no longer identical to the true volume fraction of the voids, but can be interpreted as a heuristic damage parameter. Due to its very simple form, the model has been widely used and has notably permitted to successfully reproduce both micromechanical simulations ([Tvergaard and Nielsen, 2010](#)) and experiments ([Dunand and Mohr, 2011a](#); [Xue et al., 2013](#)) under conditions of dominant shear.
- (2) The second class is based on a more micromechanical modeling of void shape effects responsible for macroscopic softening at low triaxiality. Two mathematical frameworks have been developed to derive constitutive models:
  - *Models based on limit-analysis of elementary cells:* Combination of limit-analysis and Hill-Mandel homogenization of some volume element, as first proposed by Gurson himself, permits to effectively operate the scale transition, although it only considers rigid-ideal-plastic materials. In this context, [Gologanu et al. \(1993, 1994, 1997\)](#) extended Gurson's model to spheroidal cavities, using incompressible velocity fields satisfying conditions of homogeneous boundary strain rate on all spheroids confocal with the void.<sup>2</sup> Their model has permitted to reproduce micromechanical simulations involving axisymmetric loadings under conditions of low triaxiality ([Gologanu, 1997](#); [Pardo and Hutchinson, 2000](#)). Recently, a generalization has been proposed in order to account for general ellipsoidal voids ([Madou and Leblond, 2012a, 2013b](#); [Madou et al., 2013](#)), using a family of incompressible velocity fields satisfying conditions of homogenous strain rate on an arbitrary family of confocal ellipsoids, discovered by [Leblond and Gologanu \(2008\)](#). This model has permitted to accurately reproduce micromechanical simulations of Tvergaard and co-workers ([Tvergaard, 2009, 2012](#); [Nielsen et al., 2012, 2015](#)) involving shear-dominated loadings ([Morin et al., 2016](#)).
  - *Models based on nonlinear homogenization:* Another framework, based on nonlinear homogenization, has been developed to derive constitutive equations of porous

materials from rigorous bounds for nonlinear composites ([Ponte Castañeda, 1991](#); [Willis, 1991](#); [Michel and Suquet, 1992](#)). The models derived using the so-called “variational” approach ([Ponte Castañeda and Zaidman, 1994](#); [Kailasam and Ponte Castañeda, 1998](#)) naturally account for void shape effects but severely overestimate the limit-load for predominantly hydrostatic loadings. Later, [Danas and Ponte Castañeda \(2009\)](#) developed a model based on more refined bounds that has been applied to structures subjected to shear-dominated loadings ([Danas and Aravas, 2012](#)).

The aim of this paper is to investigate ductile failure under shear-dominated loadings, using a micromechanical model of plastic porous solids incorporating void shape effects. The model selected is that developed by ([Madou and Leblond, 2012a, 2013b](#); [Madou et al., 2013](#)). This model is applied to the numerical simulation of [Dunand and Mohr \(2011a,b\)](#)'s experiments of ductile failure of “butterfly” specimens subjected to combined tension and shear.

The paper is organized as follows:

- Section 2 briefly presents [Dunand and Mohr \(2011a,b\)](#)'s experiments.
- Section 3 recapitulates the Madou-Leblond model. The primitive form of the model ([Madou and Leblond, 2012a, 2013b](#); [Madou et al., 2013](#)) is completed with heuristic extensions so as to include coalescence of voids and strain hardening, following [Morin et al. \(2016\)](#).
- In Section 4 we investigate the predictions of the Madou-Leblond model, as applied to the experiments presented in Section 2. The force-displacement curves and the location of the cracks are notably investigated.

## 2. Experimental procedures

We recall in this section the basic setup of the experiments performed by [Dunand and Mohr \(2011b, a\)](#) that we will try to reproduce with an advanced model of ductile fracture.

### 2.1. Bi-axial experiments

The bi-axial fracture experiments are performed with a dual actuator system (see [Fig. 1a](#)) that permits to apply a combination of normal and transverse loads on the edge of a “butterfly specimen”. The specimen, represented in [Fig. 1b](#), includes a gage section of reduced thickness that has been designed in such a way that fracture is prone to initiate at its center. The ratio of the vertical force  $F_V$  and the horizontal force  $F_H$  applied is characterized by the bi-axial loading angle  $\beta$  defined by

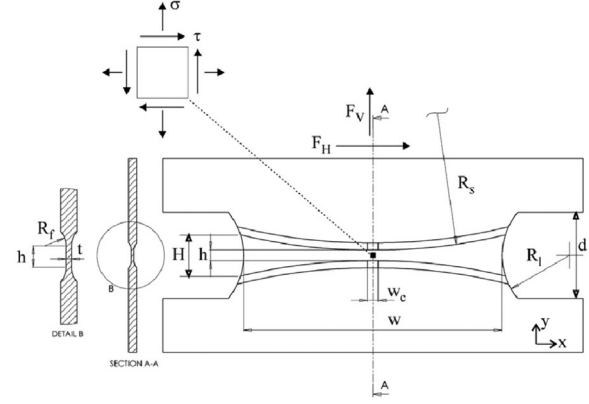
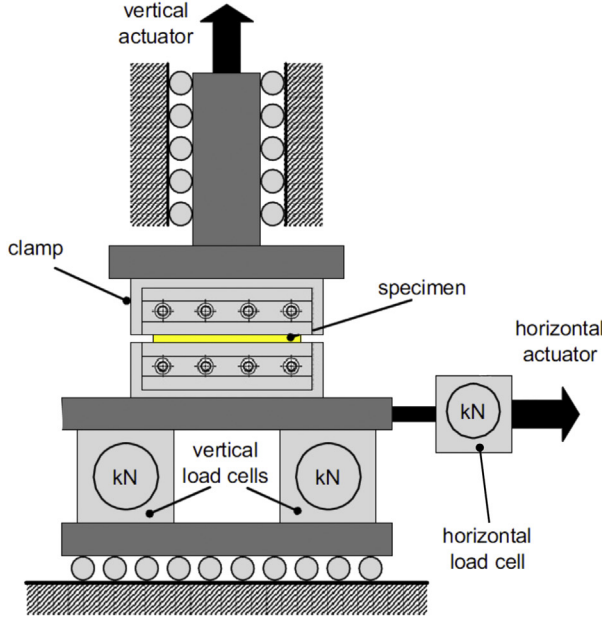
$$\tan\beta = \frac{F_V}{F_H}, \quad (1)$$

where  $\beta = 0^\circ$  corresponds to pure shear and  $\beta = 90^\circ$  to tension. Four different loading conditions are investigated:  $\beta = 0^\circ$  (pure shear),  $\beta = 25^\circ$  (shear-dominated loading),  $\beta = 63^\circ$  (tension-dominated loading) and  $\beta = 90^\circ$  (tension). The experiments are performed under force control to enforce the desired value of the loading angle  $\beta$ .

### 2.2. Material

The experiments are performed on a TRIP780 steel. This material features a complex multiphase microstructure composed of

<sup>2</sup> In a variant, [Garajeu et al. \(2000\)](#) considered a velocity field orthogonal to all such spheroids.



(a) Sketch of the dual actuator testing system (b) Geometry of the butterfly specimen

Fig. 1. The experimental setup (after Dunand and Mohr (2011a)).

ferrite, bainite and martensite. It also contains about 6% of retained austenite which may undergo phase transformation upon mechanical loading. However, the phase transformation is expected to be complete after applying a few percent of strain. Given that the fracture strains are one order of magnitude higher, we do not expect any effect of the transformation on the governing deformation process leading to ductile fracture. The elasto-plastic behavior of this 1.4 mm thick mildly-anisotropic sheet material (Lankford ratios ranging from 0.82 to 1.01) has been characterized in detail by Mohr et al. (2010).

### 2.3. Quantities investigated

For each loading case, two force-displacement curves are recorded: (i) the horizontal force versus the horizontal displacement and (ii) the vertical force versus the vertical displacement. Furthermore, photographs of the fractured (or quasi-fractured) specimens are taken in order to determine the locus of initiation of the crack (Dunand and Mohr, 2011b).

## 3. The Madou-Leblond model for plastic porous materials including void shape effects

In this section, we briefly recall the main equations defining the Madou-Leblond model along with its extension by Morin et al. (2016). The reader is referred to Madou and Leblond (2012a,b, 2013) and Madou et al. (2013) for a detailed description of all model developments.

### 3.1. Primitive form

#### 3.1.1. Preliminaries

We consider here the Madou-Leblond model (denoted ML hereafter) in its primitive form. This model applies to aligned ellipsoidal voids of identical shape and orientation. The macroscopic criterion is obtained from some approximate limit-analysis

of an ellipsoidal cell  $\Omega$  whose constitutive material obeys the isotropic von Mises criterion, containing a confocal ellipsoidal void  $\omega$  of semi-axes  $a > b > c$  oriented along the unit vectors  $\mathbf{e}_x$ ,  $\mathbf{e}_y$ ,  $\mathbf{e}_z$ . The void's surface is characterized by the quadratic form  $\mathcal{P}$  defined by

$$\mathcal{P}(\mathbf{u}) \equiv \frac{(\mathbf{u} \cdot \mathbf{e}_x)^2}{a^2} + \frac{(\mathbf{u} \cdot \mathbf{e}_y)^2}{b^2} + \frac{(\mathbf{u} \cdot \mathbf{e}_z)^2}{c^2}. \quad (2)$$

(Note that the equation of this surface is  $\mathcal{P}(\mathbf{OM}) = 1$  where  $M$  denotes the current point and  $O$  the center of the void). The matrix  $\mathbf{P} \equiv (P_{ij})$  of the quadratic form  $\mathcal{P}$  is expressed in the fixed frame  $(\mathbf{e}_1, \mathbf{e}_2, \mathbf{e}_3)$  of the observer. Since its diagonalization provides the semi-axes and the orientation of the void, it may be used to completely define the ellipsoidal void.<sup>3</sup> Finally, the porosity (void volume fraction) is denoted  $f$ .

#### 3.1.2. Macroscopic yield criterion

The ML macroscopic yield criterion reads

$$\Phi(\boldsymbol{\sigma}, \mathbf{P}, f, \sigma_0) = \frac{\mathcal{Q}(\boldsymbol{\sigma})}{\sigma_0^2} + 2(1+g)(f+g) \cosh \left[ \frac{\mathcal{L}(\boldsymbol{\sigma})}{\sigma_0} \right] - (1+g)^2 - (f+g)^2 \leq 0. \quad (3)$$

In this equation:

- $\mathcal{Q}(\boldsymbol{\sigma})$  is a quadratic form of the components of the Cauchy stress tensor  $\boldsymbol{\sigma}$  defined by

<sup>3</sup> The model does not contain any characteristic lengthscale; what matters is only the ratios of two semi-axes over the third one, not their absolute value. Thus, one semi-axis may conventionally be set to unity initially.

$$\mathcal{Q}(\boldsymbol{\sigma}) = \boldsymbol{\sigma} : \mathbf{Q} : \boldsymbol{\sigma} \quad (4)$$

where  $\mathbf{Q}$  is a fourth-order tensor;

- $\mathcal{L}(\boldsymbol{\sigma})$  is a linear form of the diagonal components of  $\boldsymbol{\sigma}$  in the basis  $(\mathbf{e}_x, \mathbf{e}_y, \mathbf{e}_z)$  defined by

$$\mathcal{L}(\boldsymbol{\sigma}) = \kappa \mathbf{H} : \boldsymbol{\sigma} \quad (5)$$

where  $\kappa$  is a scalar and  $\mathbf{H}$  a second-order tensor of unit trace;

- $g$  is the second porosity, whose value is tied to the first porosity and the shape of the void. This parameter, nil in the case of prolate voids and non-zero in the case of oblate voids, reduces to the classical “crack density” in the case of penny-shape cracks;
- $\sigma_0$  is the yield stress of the sound matrix, assumed to be constant in the primitive version of the model considered here.

The expressions of all model parameters are given in [Madou and Leblond \(2012b\)](#).

### 3.1.3. Macroscopic flow rule

Since the normality of the plastic flow rule is preserved during the homogenization procedure ([Gurson, 1977](#)), this rule necessarily reads

$$\mathbf{D}^p = \dot{\lambda} \left[ 2 \frac{\mathbf{Q} : \boldsymbol{\sigma}}{\sigma_0^2} + \frac{2}{\sigma_0} (1 + g)(f + g) \kappa \mathbf{H} \sinh \left( \frac{\kappa \mathbf{H} : \boldsymbol{\sigma}}{\sigma_0} \right) \right] , \quad (6)$$

$$\dot{\lambda} \begin{cases} = 0 & \text{if } \Phi(\boldsymbol{\sigma}, \mathbf{P}, f, \sigma_0) < 0 \\ \geq 0 & \text{if } \Phi(\boldsymbol{\sigma}, \mathbf{P}, f, \sigma_0) = 0 \end{cases}$$

where  $\mathbf{D}^p$  denotes the Eulerian plastic strain rate and  $\dot{\lambda}$  the plastic multiplier. Note that in this equation the conditions  $\dot{\lambda} \geq 0$ ,  $\Phi = 0$  defining the second possibility for the plastic multiplier implicitly cover two distinct cases: (i) elastic unloading, for which  $\dot{\lambda} = 0$  and  $\dot{\Phi} < 0$  ( $\Phi$  becomes negative immediately after the instant considered, thus ruling out plasticity); (ii) plastic loading, for which  $\dot{\lambda} \geq 0$  and  $\dot{\Phi} = 0$  (plasticity implies sustained satisfaction of the yield criterion  $\Phi = 0$ ).

### 3.1.4. Evolution equations of the internal parameters

The evolution equation of the porosity is classically deduced from the approximate incompressibility of the matrix:

$$\dot{f} = (1 - f) \text{tr}(\mathbf{D}^p). \quad (7)$$

The evolution equation of the matrix  $\mathbf{P}$  characterizing the shape and orientation of the ellipsoidal voids is given by

$$\dot{\mathbf{P}} = -\mathbf{P} \cdot (\mathbf{D}^v + \boldsymbol{\Omega}^v) - (\mathbf{D}^v + \boldsymbol{\Omega}^v)^T \cdot \mathbf{P} \quad (8)$$

where  $\mathbf{D}^v$  and  $\boldsymbol{\Omega}^v$  denote the strain- and rotation-rate tensors of the void, respectively. These rates are given by:

$$\begin{cases} \mathbf{D}^v = \mathbf{L} : \mathbf{D}^p \\ \boldsymbol{\Omega}^v = \boldsymbol{\Omega} + \mathbf{R} : \mathbf{D}^p \end{cases} \quad (9)$$

In these expressions,  $\boldsymbol{\Omega}$  is the rotation-rate tensor of the material (antisymmetric part of the velocity gradient) and  $\mathbf{L}$  and  $\mathbf{R}$  fourth-

order “localization tensors” (see [Madou et al. \(2013\)](#) for the detailed expressions of their components).

## 3.2. Extensions

Following [Morin et al. \(2016\)](#), we complete the ML model with some heuristic extensions in order to make it applicable to “real” materials and situations.

### 3.2.1. Tvergaard’s parameter

First we introduce the so-called “Tvergaard parameter” in the yield criterion (3) and the flow rule (6), in order to account for more realistic shapes of the elementary cell ([Tvergaard, 1981](#)): this is done by replacing the term  $(f + g)$  by  $q(f + g)$ , where  $q$  is a heuristic factor slightly larger than unity.

In the case of spheroidal voids, [Gologanu \(1997\)](#) considered, from various physical arguments, Tvergaard’s parameter  $q$  as a function of the void shape. Following [Morin et al. \(2016\)](#), we consider that a general ellipsoidal void of semi-axes  $a, b, c$  ( $a > b > c$ ) is “intermediate” between a prolate spheroidal void of semi-axes  $a, c, c$  and an oblate one of semi-axes  $a, a, c$ . The proposed expression of  $q$  is then an interpolation between [Gologanu \(1997\)](#)’s expressions for the prolate and oblate cases:

$$q = (1 - k)q^{\text{prol}} + kq^{\text{obl}} ,$$

$$k = \sqrt{\frac{b^2 - c^2}{a^2 - c^2}} , \quad \begin{cases} q^{\text{prol}} = 1 + (q^{\text{sph}} - 1) \left[ \frac{2a/c}{1 + (a/c)^2} \right]^{3/2} \\ q^{\text{obl}} = 1 + (q^{\text{sph}} - 1) \left[ \frac{2a/c}{1 + (a/c)^2} \right] \end{cases} \quad (10)$$

where  $q^{\text{sph}}$  represents [Tvergaard \(1981\)](#)’s original value of  $q$  for spherical voids, and  $q^{\text{prol}}$  and  $q^{\text{obl}}$  those of [Gologanu \(1997\)](#) for prolate and oblate voids.

### 3.2.2. Coalescence

In order to account for coalescence of voids, we extend [Tvergaard and Needleman \(1984\)](#)’s classical modification of [Gurson \(1977\)](#)’s model, consisting in replacing the true porosity  $f$  by some larger fictitious one  $f^*$  once some “critical value”  $f_c$  has been reached. Since in the ML model the parameter governing softening is no longer  $f$  but  $f + g$ , it is natural to apply the modification to this parameter and thus replace it by

$$(f + g)^* = \begin{cases} f + g & \text{if } f + g \leq (f + g)_c \\ (f + g)_c + \delta[(f + g) - (f + g)_c] & \text{if } f + g > (f + g)_c \end{cases} \quad (11)$$

where  $(f + g)_c$  and  $\delta > 1$  are material parameters.

### 3.2.3. Strain hardening

Finally, strain hardening is introduced following [Gurson \(1977\)](#)’s approach. The constant yield limit  $\sigma_0$  in the criterion (3) is thus replaced by some “average yield stress”  $\bar{\sigma}$  given by:

$$\bar{\sigma} \equiv \sigma(\bar{\epsilon}) \quad (12)$$

where  $\sigma(\epsilon)$  is the function which provides the local yield limit as a function of the local cumulated plastic strain  $\epsilon$ , and  $\bar{\epsilon}$  represents some “average equivalent strain” in the sound matrix. The



evolution of  $\bar{\varepsilon}$  is governed by the following equation:

$$(1-f)\bar{\sigma}\dot{\bar{\varepsilon}} = \boldsymbol{\sigma} : \mathbf{D}^p \quad (13)$$

which expresses the heuristic assumption that the plastic dissipation in the heterogeneous porous material,  $\boldsymbol{\sigma} : \mathbf{D}^p$ , is equal to that in a fictitious “equivalent” homogeneous material with equivalent strain  $\bar{\varepsilon}$  and yield stress  $\bar{\sigma}$ ,  $(1-f)\bar{\sigma}\dot{\bar{\varepsilon}}$ .

### 3.2.4. Final form of the yield criterion and flow rule

With the above modifications in place, the final form of the ML yield criterion and its flow rule reads:

$$\begin{aligned} \Phi(\boldsymbol{\sigma}, \mathbf{P}, f, \bar{\sigma}) &= \frac{\mathcal{Q}(\boldsymbol{\sigma})}{\bar{\sigma}^2} + 2q(1+g)(f+g)^* \cosh\left[\frac{\mathcal{L}(\boldsymbol{\sigma})}{\bar{\sigma}}\right] - (1+g)^2 \\ &\quad - q^2(f+g)^{*2} \\ &\leq 0; \end{aligned} \quad (14)$$

$$\begin{aligned} \mathbf{D}^p &= \dot{\lambda} \left[ 2 \frac{\mathbf{Q} : \boldsymbol{\sigma}}{\bar{\sigma}^2} + \frac{2}{\bar{\sigma}} q(1+g)(f+g)^* \kappa \mathbf{H} \sinh\left(\frac{\kappa \mathbf{H} : \boldsymbol{\sigma}}{\bar{\sigma}}\right) \right], \\ \dot{\lambda} &\begin{cases} = 0 & \text{if } \Phi(\boldsymbol{\sigma}, \mathbf{P}, f, \bar{\sigma}) < 0 \\ \geq 0 & \text{if } \Phi(\boldsymbol{\sigma}, \mathbf{P}, f, \bar{\sigma}) = 0. \end{cases} \end{aligned} \quad (15)$$

Note again that the second possibility for  $\dot{\lambda}$  here covers both elastic unloading and plastic loading.

### 3.3. Damage parameter definition for post-processing

In the ML model, damage in the porous material results from a combination of porosity and void shape effects (through the second porosity). It is interesting to define a *single* damage parameter  $d$ , tied to both  $f$  and  $g$ , characterizing the gradual degradation of the material. This parameter does not play any role in the constitutive equations, but may be examined in a post-treatment of the results to evaluate the location and importance of damage in the structure.

Suppose that the material is entirely ruined ( $\sigma = 0$ ); one then obtains from the criterion (14):

$$\begin{aligned} 2q(1+g)(f+g)^* - (1+g)^2 - q^2(f+g)^{*2} \\ = -[1+g-q(f+g)^*]^2 = 0. \end{aligned} \quad (16)$$

It follows that  $q(f+g)^* = 1+g$ . The damage parameter  $d$  can thus be defined by the formula:

$$d = \frac{q(f+g)^*}{1+g}, \quad (17)$$

the values  $d = 0$  and  $d = 1$  corresponding to absence of damage and total damage, respectively.

## 4. Comparison between experiments and numerical results

### 4.1. Description of the numerical simulations

#### 4.1.1. Mesh and boundary conditions

We consider one half of the butterfly specimen, the upper and bottom edges of which are subjected to uniform displacements  $u_x$  and  $u_y$ , respectively (see Fig. 2). The displacements are adjusted so as to enforce the desired loading angle  $\beta$  defined by equation (1). The mesh is composed of 71,986 elements and 82,479 nodes; we use selectively subintegrated 8-node trilinear brick and 6-node

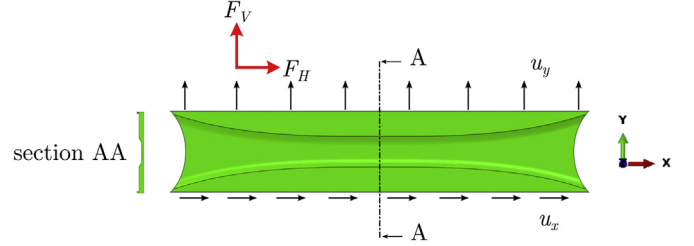


Fig. 2. Boundary conditions considered in the numerical simulations.

trilinear wedge elements well suited to quasi-incompressible plasticity. The use of Gurson-type models is known to raise the issue of mesh dependency when softening occurs (see e.g. Tvergaard and Needleman (1984); Besson et al. (2001)). In the absence of a regularization of some sort (such as use of a nonlocal evolution equation of the porosity (Enakoutsa et al., 2007) or a second-gradient model (Gologanu et al., 1997)), a classical heuristic “solution” to the problem is to ascribe a value of the order of the void spacing to the mesh size (see e.g. Bergheau et al. (2014)). In the present case, in the gage section of the specimen, the mesh considered is composed of 210 elements in the direction  $x$ , 60 elements in the direction  $y$  and 8 elements in the direction  $z$ , respectively (see Fig. 2). This discretization is identical to that used by Dunand and Mohr (2011a) in the case of Nahshon and Hutchinson (2008)’s model. The simulations are performed with the commercial finite element code ABAQUS, using a UMAT subroutine based on the numerical implementation of the ML model developed by Morin et al. (2016) and made freely available on the Web (see Leblond (2015)).

#### 4.1.2. Parameters used in the ML model

For the elastic properties we consider the values given by Dunand and Mohr (2011b) (see Table 1). The hardening law considered is also that calibrated by Dunand and Mohr (2011b) and is given by the following modified Swift law:

$$\sigma(\varepsilon) = K(\varepsilon + \varepsilon_0)^n \quad (18)$$

where the values of the parameters  $K$ ,  $\varepsilon_0$  and  $n$  are given in Table 1.

The more tricky part concerns the parameters related to damage (initial porosity, initial shape of the voids and coalescence parameters). According to Uthaisangskuk et al. (2009), there are two populations of cavities in a TRIP600 steel<sup>4</sup>: (i) an initial population, with porosity  $6 \times 10^{-4}$ , and (ii) a second population of voids nucleated after some deformation, with initial porosity  $5 \times 10^{-2}$ . Since we do not consider continuous nucleation in the present model, we must consider some intermediate initial porosity. We thus consider the average value  $f_0 = 5 \times 10^{-3}$  permitting to account for continuously nucleated voids, which is reasonable for metallic alloys. Furthermore in TRIP600 steels, the primary population of voids results from the decohesion between the matrix and non-metallic soft MnS inclusions (Uthaisangskuk et al., 2009). For such a mechanism it is reasonable to assume that the initial voids are spherical, so that the initial matrix  $\mathbf{P}_0$  is a multiple of the identity matrix. Note in addition that the initial void shape has, in general, little influence on softening in shear provided that the ratio between the semi-axes does not differ too much from unity (Tvergaard, 2015). Finally, we need to specify the values of the

<sup>4</sup> Since the TRIP600 and TRIP780 steels are very close from a microstructural point of view, it is reasonable to consider that the values determined experimentally by Uthaisangskuk et al. (2009) for TRIP600 also apply to TRIP780.

coalescence parameters. The calibration of parameters is based on the comparison of the predictions of the ML model and the results of some micromechanical cell calculations of Tvergaard and co-workers (Morin et al., 2016). For initially spherical voids, the ratio between the “critical” porosity  $(f + g)_c$  and the initial one  $f_0$  was found to be between 2 and 3. We adopt here the value  $(f + g)_c = 10^{-2}$  in all simulations, which corresponds to a ratio of 2 between the critical and initial porosities. This value is the minimum one in the interval  $[2, 3]$  determined by Morin et al. (2016), in compliance with the well-known observation that the “best” critical porosity values for reproduction of actual experiments tend to be slightly lower than those determined from micromechanical simulations (see e.g. Bergheau et al. (2014)). Also, we adopt the values  $\delta = [4; 4; 9; 9]$  for the cases  $\beta = [90^\circ; 63^\circ; 25^\circ; 0^\circ]$  respectively. The value used for shear-dominated loadings is consistent with that calibrated on the basis of shear-dominated micromechanical simulations (see Morin et al. (2016)), and that used for tension-dominated loadings is consistent with classical values adopted in the literature in the absence of shear (see e.g. Besson et al. (2001)).

A summary of all the parameters used is given in Table 1.

**Table 1**  
Values of parameters for the Madou-Leblond model.

$E$ [MPa]	$\nu$ [-]	$f_0$ [-]	$P_{0ij}$ [-]	$q$ [-]	$(f + g)_c$ [-]	$\delta$ [-]	$K$ [MPa]	$\epsilon_0$ [-]	$n$ [-]
185,000	0.3	$5 \times 10^{-3}$	$\delta_{ij}$	1.5	$10^{-2}$	[4; 9]	1460	$1.63 \times 10^{-3}$	0.204

## 5. Results

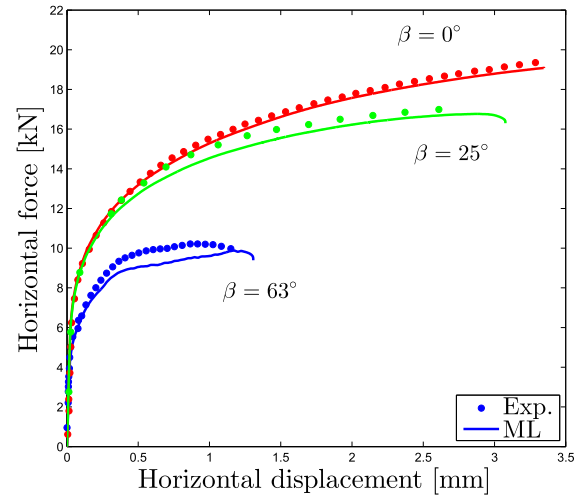
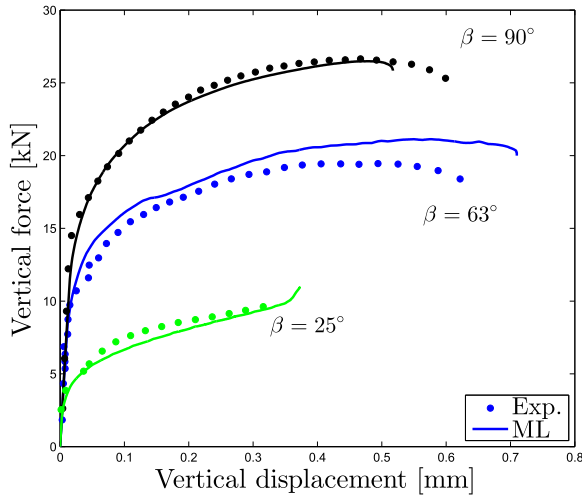
### 5.1. Force-displacement curves

The force-displacement curves are provided in Fig. 3a–b. Globally speaking, the experimental results are well reproduced by

the ML model, in all cases considered. In particular the magnitude of the force, the gradual softening and the final failure of the specimen are qualitatively well reproduced by the model for all values of  $\beta$ .

Some more detailed comments are in order:

- In all cases considered, the numerical forces do not perfectly coincide with the experimental ones, even at the beginning of the plastic phase. The small difference is a result of:
  - \* The choice of the value of the initial porosity  $f_0$ . Indeed, the value adopted is probably not optimal since we considered some average value between initially present and continuously nucleated voids. An optimization should be possible to get the best possible fit between numerical and experimental curves, but has not been attempted.
  - \* The hypothesis of a plastically isotropic von Mises matrix made in the ML model. Indeed, the material used in the experiments cannot be considered as totally isotropic, as shown by Dunand and Mohr (2011b), who modeled it with an isotropic von Mises yield function and a non-associated Hill (1948) flow rule.
- The final failure of the material observed numerically, corresponding to the end of the simulations, does not occur exactly when it is observed experimentally. The slight difference can be explained by the heuristic modeling of coalescence based on Tvergaard and Needleman (1984)’s approach, and notably the use of the same value of the heuristic parameter parameter  $(f + g)_c$  for all the loading cases. A possible way to improve the predictions of the model would be to adjust the value of this parameter according to the loading case considered, or to consider a more advanced model to describe coalescence.
- The very final stage of the fracture process is unstable, both experimentally and numerically. In the numerical simulations the final softening is brutal (see Fig. 4a–f), the slope of the force-displacement curve becoming vertical. It is remarkable that the instability observed experimentally is thus reproduced in the numerical simulations.



(a) Vertical force versus vertical displacement

(b) Horizontal force versus horizontal displacement

**Fig. 3.** Force-displacement response: experimental results (Exp.) and predictions of Madou-Leblond’s model (ML).

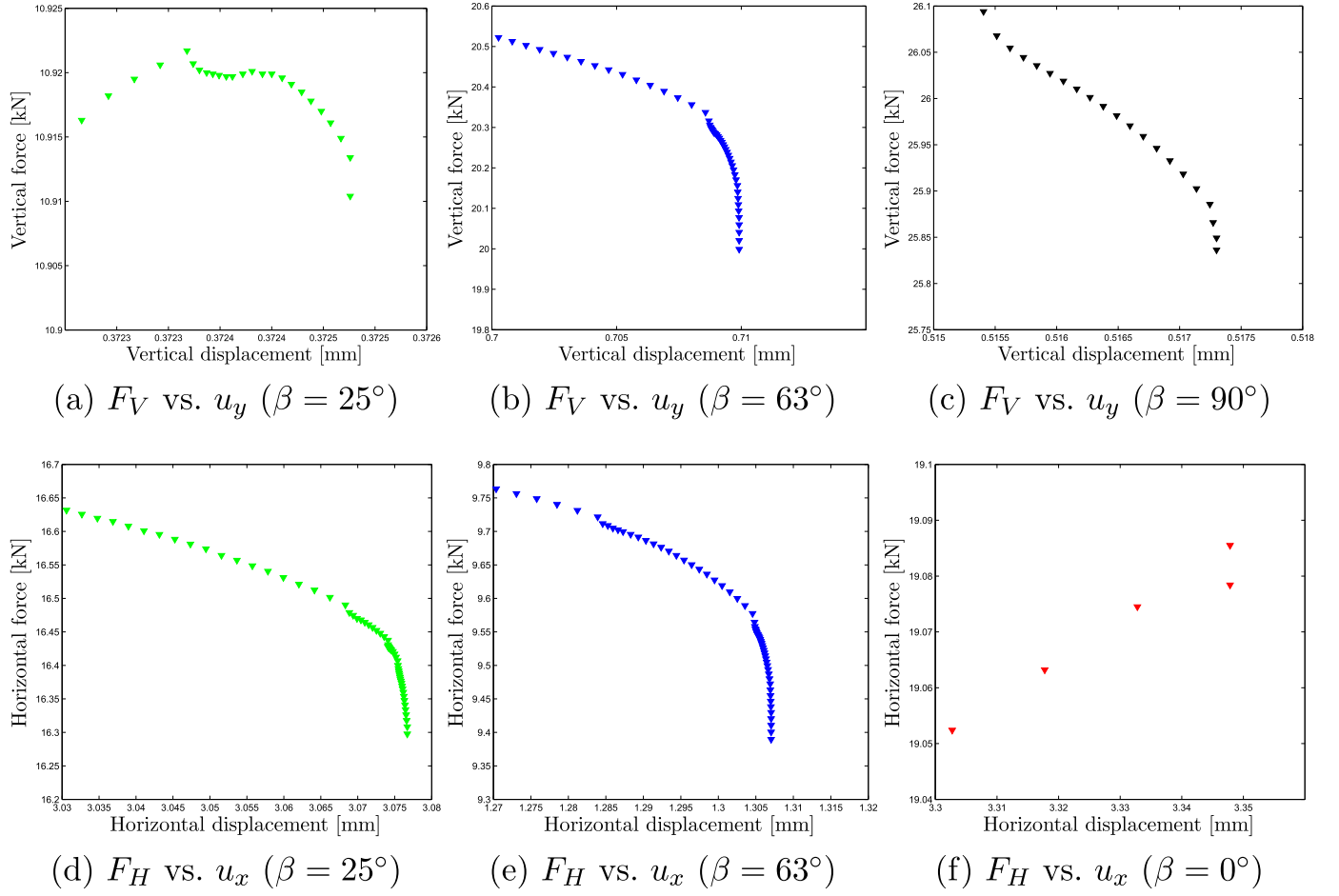
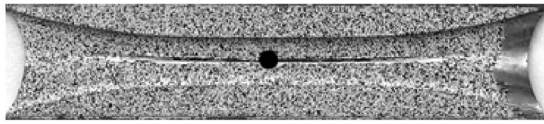
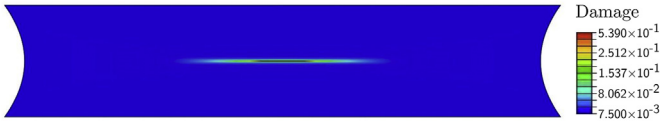


**Fig. 4.** Complementary results for the force-displacement curves: zoom on the final stage of the numerical simulations.



(a) Photograph of the quasi-fractured specimen (after Dunand and Mohr (2011b))

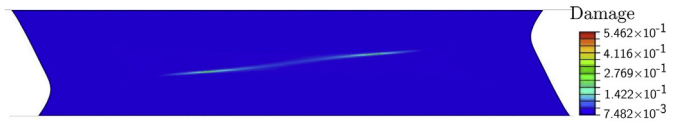


(b) Distribution of the damage parameter at the center of the specimen

**Fig. 5.** Location of the crack in the case  $\beta = 90^\circ$ .

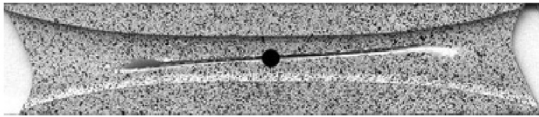


(a) Photograph of the fractured specimen (after Dunand and Mohr (2011b))

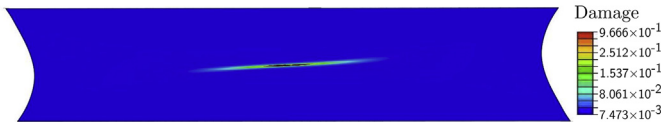


(b) Distribution of the damage parameter at the center of the specimen

**Fig. 7.** Location of the crack in the case  $\beta = 25^\circ$ .

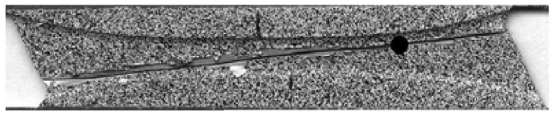


(a) Photograph of the quasi-fractured specimen (after Dunand and Mohr (2011b))

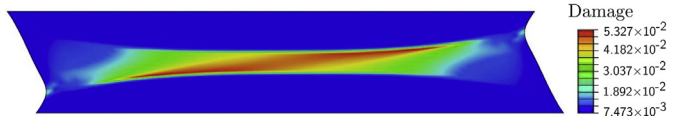


(b) Distribution of the damage parameter at the center of the specimen

**Fig. 6.** Location of the crack in the case  $\beta = 63^\circ$ .



(a) Photograph of the fractured specimen (after Dunand and Mohr (2011b))



(b) Distribution of the damage parameter at the center of the specimen

**Fig. 8.** Location of the crack in the case  $\beta = 0^\circ$ .



### 5.2. Location of the crack

The location of crack initiation is represented in Figs. 5–8, for  $\beta = [90^\circ; 63^\circ; 25^\circ; 0^\circ]$  respectively. In particular, we provide in each case: (a) a photograph of the fully or partially fractured specimen; and (b) the distribution of the damage parameter  $d$  defined by equation (17) half-way through the thickness of the specimen at the end of the numerical simulation. For completeness, we also represent the distribution of the damage parameter and the deformed mesh in section AA (defined in Fig. 2) in Fig. 9a and b at the end of the numerical simulation, in the sole case  $\beta = 63^\circ$ ; this notably permits to observe the necking of the specimen. The location of the crack is globally well reproduced by the ML model.

Again, more detailed comments are in order:

- In all the simulations, damage starts growing at the center of the specimen with very high values in some cases (see Fig. 9a). This suggests that the crack initiates at the center of the specimen and then propagates toward the free boundary.
- In the case  $\beta = 0^\circ$ , the distribution of the damage parameter is more diffuse than in the other cases: the “crack” is more a damaged zone than a truly localized crack. However, the numerical simulation still ultimately becomes unstable (see Fig. 4f), emphasizing that failure is still reached.
- It is not possible to numerically get a long crack like in the experiments (that is a large zone where  $d = 1$ ) because the simulations become unstable and stop. A complete simulation of the experiments would require incorporation of dynamic effects (inertia forces) during the final brutal drop of the load.

### 5.3. Comparison with the predictions of Gurson's model

In order to assess the importance of void shape effects on shear-dominated fracture, it is interesting to investigate the predictions of

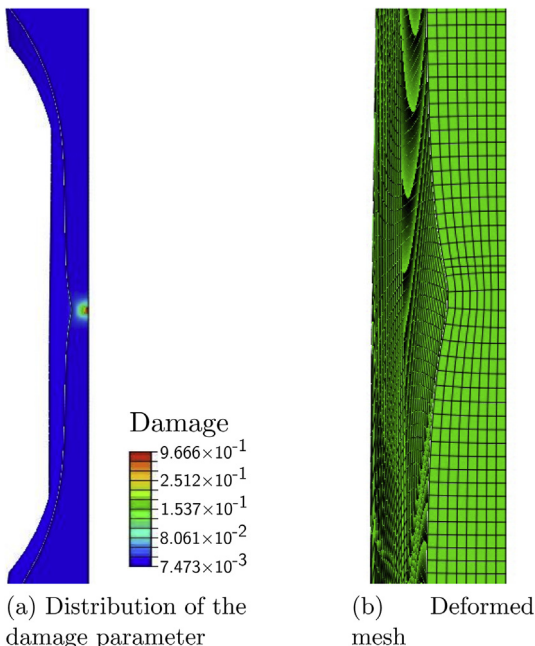


Fig. 9. Complementary results for  $\beta = 63^\circ$  in the section AA.

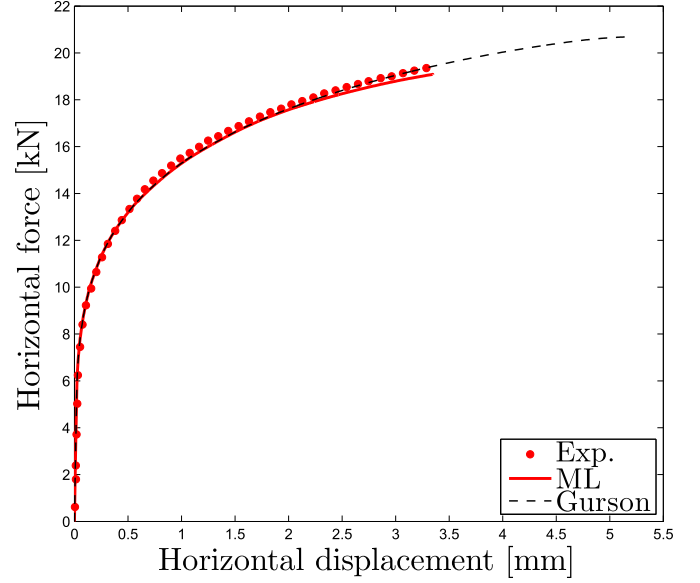


Fig. 10. Horizontal force versus horizontal displacement in the case  $\beta = 0^\circ$ : experimental results (Exp.), predictions of Madou-Leblond's model (ML) and predictions of Gurson's model (Gurson).

Gurson (1977)'s model disregarding void shape effects, in the case  $\beta = 0^\circ$ .<sup>5</sup> The horizontal force-displacement curve and the distribution of the damage parameter (identical in this case to  $qf^*$  since  $g = 0$ ) at the instant corresponding to the end of the simulation based on the ML model (i.e. at  $u_x \approx 3.4$  mm) are represented in Figs. 10 and 11 respectively.

It may be observed that Gurson's model does not predict any failure because no instability occurs; this is true even when the numerical simulation is pursued by prescribing larger horizontal displacements (this is not shown in the figures). Also, the damage parameter does not increase significantly, in contrast with what occurs with the ML model. The reason why Gurson's model predicts lower damage levels than the ML model is that the porosity does not increase for shear loadings. In other words, for such loadings the damage is mainly due to void shape effects disregarded in Gurson's model.

## 6. Discussion

Globally speaking, the ML model has permitted to accurately reproduce the experiments of ductile fracture under combined tension and shear. The macroscopic softening as well as the location of cracks are well reproduced for various loading conditions ranging from tension to pure shear. The comparison with Gurson's model has highlighted the importance of void shape effects on the progressive degradation of the material.

It should however be noted that other authors, using other models, have considered the same experiments:

- Dunand and Mohr (2011a) using Nahshon and Hutchinson (2008)'s heuristic modification of Gurson's model. The macroscopic softening was well reproduced with values of parameters in the range recommended by Nahshon and Hutchinson (2008). Crack locations were however not provided so it is not clear whether the model can correctly reproduce the initiation of cracks.

<sup>5</sup> It is worth noting that no subroutine has been developed for Gurson (1977)'s model: we have simply adapted the UMAT for the ML model by deleting the instructions pertaining to the update of the voids' shape and orientation. The initially spherical voids then remain spherical throughout the simulation.

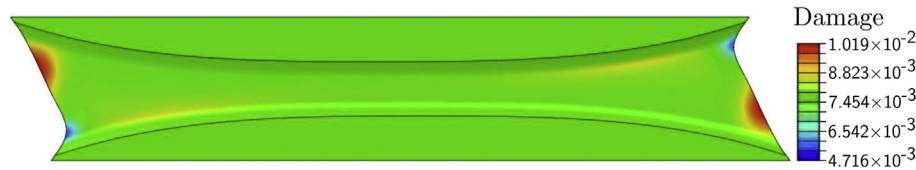


Fig. 11. Distribution of the damage parameter at  $u_x \approx 3.4$  mm in the case  $\beta = 0^\circ$ , using Gurson's model.

- Danas and Aravas (2012) using Danas and Ponte Castañeda (2009)'s model. In their simulations, they observed some softening as well as the location of cracks. However, they did not use the material properties of the TRIP780 steel, nor did they compare the model predictions to the observations.

## 7. Conclusion

The topic of this paper was the theoretical prediction of ductile failure under shear-dominated loadings. The predictions of the Madou-Leblond (ML) model (Madou and Leblond, 2012a, 2013b; Madou et al., 2013) incorporating void shape effects were compared with the experimental results of Dunand and Mohr (2011a,b) obtained on "butterfly" specimens subjected to various loadings.

The ML model has permitted to reproduce accurately the major features of all experiments, notably the macroscopic softening under shear-dominated loadings as well as the location of cracks. These results, together with those of Morin et al. (2016) on the comparison of the predictions of the ML model and the results of micromechanical simulations under shear-dominated loadings of Tvergaard and co-workers (Nielsen et al., 2012; Tvergaard, 2015), demonstrate the capabilities of the ML model for prediction of ductile failure at low stress triaxiality, notably in the presence of intense shear. The ML model thus stands as a viable, more micromechanically-based although more complex, alternative to Nahshon and Hutchinson (2008)'s modification of Gurson (1977)'s model for the description of ductile damage at low stress triaxialities.

The ML model can however be improved in order to reproduce more accurately the experimental results considered here. Several directions can be explored in this respect:

- *Coalescence of voids.* The modeling of coalescence considered in this work is a straightforward extension of Tvergaard and Needleman (1984)'s heuristic approach. It does not rely on a micromechanical basis and needs a calibration of parameters. An alternative approach would consist of using a micromechanical model of coalescence for ellipsoidal voids subjected to combined tension and shear. But such a general model of coalescence is at present lacking, although the case of spheroidal voids has been considered in recent works of Tekoglu et al. (2012) and Torki et al. (2015).
- *Plastic anisotropy of the matrix.* The ML model applies to plastically isotropic matrices, while the material used in the experiments is mildly anisotropic. It would be interesting to consider instead a model for plastic porous materials incorporating a coupling between plastic anisotropy of the matrix and void shape effects (see e.g. Monchiet et al. (2008); Keralavarma and Benzerga (2010); Morin et al. (2015)).

## References

Barsoum, I., Faleskog, J., 2007a. Rupture mechanisms in combined tension and shear—Experiments. *Int. J. Solids Struct.* 44, 1768–1786.

Barsoum, I., Faleskog, J., 2007b. Rupture mechanisms in combined tension and shear—Micromechanics. *Int. J. Solids Struct.* 44, 5481–5498.

Benzerga, A.A., Leblond, J.B., 2010. Ductile fracture by void growth to coalescence. *Adv. Appl. Mech.* 44, 169–305.

Bergheau, J.M., Leblond, J.B., Perrin, G., 2014. A new numerical implementation of a second-gradient model for plastic porous solids, with an application to the simulation of ductile rupture tests. *Comput. Methods Appl. Mech. Eng.* 268, 105–125.

Besson, J., Steglich, D., Brocks, W., 2001. Modeling of crack growth in round bars and plane strain specimens. *Int. J. Solids Struct.* 38, 8259–8284.

Danas, K., Aravas, N., 2012. Numerical modeling of elasto-plastic porous materials with void shape effects at finite deformations. *Compos. Part B Eng.* 43, 2544–2559.

Danas, K., Ponte Castañeda, P., 2009. A finite-strain model for anisotropic viscoplastic porous media: I – Theory. *Eur. J. Mech. - A/Solids* 28, 387–401.

Dunand, M., Mohr, D., 2011a. On the predictive capabilities of the shear modified Gurson and the modified Mohr–Coulomb fracture models over a wide range of stress triaxialities and Lode angles. *J. Mech. Phys. Solids* 59, 1374–1394.

Dunand, M., Mohr, D., 2011b. Optimized butterfly specimen for the fracture testing of sheet materials under combined normal and shear loading. *Eng. Fract. Mech.* 78, 2919–2934.

Dunand, M., Mohr, D., 2014. Effect of Lode parameter on plastic flow localization after proportional loading at low stress triaxialities. *J. Mech. Phys. Solids* 66, 133–153.

Enakoutsa, K., Leblond, J., Perrin, G., 2007. Numerical implementation and assessment of a phenomenological nonlocal model of ductile rupture. *Comput. Methods Appl. Mech. Eng.* 196, 1946–1957.

Faleskog, J., Barsoum, I., 2013. Tension–torsion fracture experiments—Part I: experiments and a procedure to evaluate the equivalent plastic strain. *Int. J. Solids Struct.* 50, 4241–4257.

Garajeu, M., Michel, J.C., Suquet, P., 2000. A micromechanical approach of damage in viscoplastic materials by evolution in size, shape and distribution of voids. *Comput. Methods Appl. Mech. Eng.* 183, 223–246.

Ghahremaninezhad, A., Ravi-Chandar, K., 2013. Ductile failure behavior of polycrystalline Al 6061-T6 under shear dominant loading. *Int. J. Fract.* 180, 23–39.

Gologanu, M., 1997. Etude de quelques problèmes de rupture ductile des métaux. Ph.D. thesis. Université Paris, p. 6.

Gologanu, M., Leblond, J.B., Devaux, J., 1993. Approximate models for ductile metals containing non-spherical voids—Case of axisymmetric prolate ellipsoidal cavities. *J. Mech. Phys. Solids* 41, 1723–1754.

Gologanu, M., Leblond, J.B., Devaux, J., 1994. Approximate models for ductile metals containing nonspherical voids—Case of axisymmetric oblate ellipsoidal cavities. *J. Eng. Mater. Technol.* 116, 290–297.

Gologanu, M., Leblond, J.B., Perrin, G., Devaux, J., 1997. Recent extensions of Gurson's model for porous ductile metals. In: Suquet, P. (Ed.), *Continuum Micromechanics*. Springer Verlag, New-York, pp. 61–130.

Graham, S.M., Zhang, T., Gao, X., Hayden, M., 2012. Development of a combined tension–torsion experiment for calibration of ductile fracture models under conditions of low triaxiality. *Int. J. Mech. Sci.* 54, 172–181.

Gurson, A.L., 1977. Continuum theory of ductile rupture by void nucleation and growth: Part I—Yield criteria and flow rules for porous ductile media. *ASME J. Eng. Mater. Technol.* 99, 2–15.

Halton, S.S., Kyriakides, S., Ravi-Chandar, K., 2013. Ductile failure under combined shear and tension. *Int. J. Solids Struct.* 50, 1507–1522.

Hill, R., 1948. A theory of the yielding and plastic flow of anisotropic metals. *Proc. R. Soc. Lond. A* 193, 281–297.

Kailasam, M., Ponte Castañeda, P., 1998. A general constitutive theory for linear and nonlinear particulate media with microstructure evolution. *J. Mech. Phys. Solids* 46, 427–465.

Keralavarma, S., Benzerga, A., 2010. A constitutive model for plastically anisotropic solids with non-spherical voids. *J. Mech. Phys. Solids* 58, 874–901.

Koplik, J., Needleman, A., 1988. Void growth and coalescence in porous plastic solids. *Int. J. Solids Struct.* 24, 835–853.

Leblond, J.B., 2015. UMAT, available at: the address. : [www.dalembert.upmc.fr/home/leblond/](http://www.dalembert.upmc.fr/home/leblond/).

Leblond, J.B., Gologanu, M., 2008. External estimate of the yield surface of an arbitrary ellipsoid containing a confocal void. *Comptes Rendus Mécanique* 336, 813–819.

Leblond, J.B., Mottet, G., 2008. A theoretical approach of strain localization within thin planar bands in porous ductile materials. *Comptes Rendus Mécanique* 336, 176–189.

Madou, K., Leblond, J.B., 2012a. A Gurson-type criterion for porous ductile solids

- containing arbitrary ellipsoidal voids—I: limit-analysis of some representative cell. *J. Mech. Phys. Solids* 60, 1020–1036.
- Madou, K., Leblond, J.B., 2012b. A Gurson-type criterion for porous ductile solids containing arbitrary ellipsoidal voids—II: determination of yield criterion parameters. *J. Mech. Phys. Solids* 60, 1037–1058.
- Madou, K., Leblond, J.B., 2013. Numerical studies of porous ductile materials containing arbitrary ellipsoidal voids—I: yield surfaces of representative cells. *Eur. J. Mech. - A/Solids* 42, 480–489.
- Madou, K., Leblond, J.B., Morin, L., 2013. Numerical studies of porous ductile materials containing arbitrary ellipsoidal voids—II: evolution of the length and orientation of the void axes. *Eur. J. Mech. - A/Solids* 42, 490–507.
- McClintock, F.A., 1968. A criterion for ductile fracture by the growth of holes. *J. Appl. Mech.* 35, 363–371.
- Michel, J.C., Suquet, P., 1992. The constitutive law of nonlinear viscous and porous materials. *J. Mech. Phys. Solids* 40, 783–812.
- Mohr, D., Dunand, M., Kim, K.H., 2010. Evaluation of associated and non-associated quadratic plasticity models for advanced high strength steel sheets under multi-axial loading. *Int. J. Plast.* 26, 939–956.
- Mohr, D., Henn, S., 2007. Calibration of stress-triaxiality dependent crack formation criteria: a new hybrid experimental–numerical method. *Exp. Mech.* 47, 805–820.
- Monchiet, V., Cazacu, O., Charkaluk, E., Kondo, D., 2008. Macroscopic yield criteria for plastic anisotropic materials containing spheroidal voids. *Int. J. Plast.* 24, 1158–1189.
- Morin, L., Leblond, J.B., Kondo, D., 2015. A Gurson-type criterion for plastically anisotropic solids containing arbitrary ellipsoidal voids. *Int. J. Solids Struct.* 77, 86–101.
- Morin, L., Leblond, J.B., Tvergaard, V., 2016. Application of a model of plastic porous materials including void shape effects to the prediction of ductile failure under shear-dominated loadings. *J. Mech. Phys. Solids* 94, 148–166.
- Nahshon, K., Hutchinson, J.W., 2008. Modification of the Gurson model for shear failure. *Eur. J. Mech. - A/Solids* 27, 1–17.
- Nielsen, K.L., Dahl, J., Tvergaard, V., 2012. Collapse and coalescence of spherical voids subject to intense shearing: studied in full 3D. *Int. J. Fract.* 177, 97–108.
- Papasidero, J., Doquet, V., Mohr, D., 2015. Ductile fracture of aluminum 2024-T351 under proportional and non-proportional multi-axial loading: bao–Wierzbicki results revisited. *Int. J. Solids Struct.* 69–70, 459–474.
- Pardoën, T., Hutchinson, J.W., 2000. An extended model for void growth and coalescence. *J. Mech. Phys. Solids* 48, 2467–2512.
- Pineau, A., Benzerga, A.A., Pardoën, T., 2016. Failure of metals I: brittle and ductile fracture. *Acta Mater.* 107, 424–483.
- Ponte Castañeda, P., 1991. The effective mechanical properties of nonlinear isotropic composites. *J. Mech. Phys. Solids* 39, 45–71.
- Ponte Castañeda, P., Zaidman, M., 1994. Constitutive models for porous materials with evolving microstructure. *J. Mech. Phys. Solids* 42, 1459–1497.
- Rice, J.R., Tracey, D.M., 1969. On the ductile enlargement of voids in triaxial stress fields. *J. Mech. Phys. Solids* 17, 201–217.
- Scheyvaerts, F., Onck, P.R., Tekoglu, C., Pardoën, T., 2011. The growth and coalescence of ellipsoidal voids in plane strain under combined shear and tension. *J. Mech. Phys. Solids* 59, 373–397.
- Tekoglu, C., Leblond, J.B., Pardoën, T., 2012. A criterion for the onset of void coalescence under combined tension and shear. *J. Mech. Phys. Solids* 60, 1363–1381.
- Torki, M.E., Benzerga, A.A., Leblond, J.B., 2015. On void coalescence under combined tension and shear. *J. Appl. Mech.* 82, 071005.
- Tvergaard, V., 1981. Influence of voids on shear band instabilities under plane strain conditions. *Int. J. Fract.* 17, 389–407.
- Tvergaard, V., 2009. Behaviour of voids in a shear field. *Int. J. Fract.* 158, 41–49.
- Tvergaard, V., 2012. Effect of stress-state and spacing on voids in a shear-field. *Int. J. Solids Struct.* 49, 3047–3054.
- Tvergaard, V., 2015. Effect of initial void shape on ductile failure in a shear field. *Mech. Mater.* 90, 2–9.
- Tvergaard, V., Needleman, A., 1984. Analysis of the cup-cone fracture in a round tensile bar. *Acta Metall.* 32, 157–169.
- Tvergaard, V., Nielsen, K.L., 2010. Relations between a micro-mechanical model and a damage model for ductile failure in shear. *J. Mech. Phys. Solids* 58, 1243–1252.
- Uthaisangsuk, V., Pohl, U., Bleck, W., 2009. Characterisation of formability behaviour of multiphase steels by micromechanical modelling. *Int. J. Fract.* 157, 55–69.
- Willis, J.R., 1991. On methods for bounding the overall properties of nonlinear composites. *J. Mech. Phys. Solids* 39, 73–86.
- Xue, L., 2008. Constitutive modeling of void shearing effect in ductile fracture of porous materials. *Eng. Fract. Mech.* 75, 3343–3366.
- Xue, Z., Faleskog, J., Hutchinson, J.W., 2013. Tension–torsion fracture experiments – Part II: simulations with the extended Gurson model and a ductile fracture criterion based on plastic strain. *Int. J. Solids Struct.* 50, 4258–4269.